Rheinische Friedrich-Wilhelms-Universität Bonn


# BACHELOR THESIS

## INVESTIGATION OF THE GALACTIC WNE STARS


| | |
|---|---|
| Author: | Daniel Pauli |
| Student-ID: | 2864448 |
| Degree Courses: | Physics |
| corrected by: | Prof. Dr. Norbert Langer |
| and by: | Prof. Dr. Thomas Reiprich |


Bonn, August 13, 2018

## Declaration of Authorship

I hereby declare that the thesis submitted is my own unaided work. All direct or indirect sources used are acknowledged as references.

I am aware that the thesis in digital form can be examined for the use of unauthorized aid and in order to determine whether the thesis as a whole or parts incorporated in it may be deemed as plagiarism. For the comparison of my work with existing sources I agree that it shall be entered in a database where it shall also remain after examination, to enable comparison with future theses submitted. Further rights of reproduction and usage, however, are not granted here.

This paper was not previously presented to another examination board and has not been published.

place, date

signature

**Abstract**

*Context.* Stellar evolution codes use the mass of a star as initial parameter. With this given information and the stellar structure equations it is possible to predict the evolution of stars. But hydrogen free Wolf-Rayet stars which are predicted to lie near the helium zero-age-main-sequence, do not fulfill the predictions of stellar models. Wolf-Rayet stars have strong line driven winds and strong mass-loss rates, which are greatly dependent on the metallicity of the star.

*Aims.* In this thesis we wish to find out if the metallicity should be considered as second initial parameter for stellar models of hydrogen free Wolf-Rayet stars. The temperature will be investigated as function of mass and metallicity.

*Methods.* To achieve this goal, the present-day radial metallicity gradient of the galaxy has been estimated. Using new distances from the Gaia Data Release 2 (Gaia Collaboration et al., 2018) corrections in luminosity, mass and mass-loss rate for all hydrogen free Wolf-Rayet stars are derived. The temperatures have been adopted from Hamann et al. (2006), who made precise line blanked atmospheric models.

*Result.* The mass-loss luminosity relation has been investigated and confirmed a correlation between the mass-loss rate, luminosity and the metallicity. The temperature of Wolf-Rayet stars turned out to be a function of mass and metallicity. As a consequence the metallicity should be considered as second initial parameter for hydrogen free Wolf-Rayet star models.

# Contents

## List of Figures



## List of Tables

# 1 Introduction

Stars and stellar evolution theory teaches that the behavior of a star follows the stellar structure equations.

$$
\begin{aligned}
\frac{\partial r}{\partial m} &= \frac{1}{4\pi r^2 \rho} \\
\frac{\partial P}{\partial m} &= -\frac{Gm}{4\pi r^4} - \frac{1}{4\pi r^2}\frac{\partial^2 r}{\partial t^2} \\
\frac{\partial l}{\partial m} &= \epsilon_{nuc} - \epsilon_\nu - T\frac{\partial s}{\partial t} \\
\frac{\partial T}{\partial m} &= -\frac{Gm}{4\pi r^4}\frac{T}{P}\cdot\nabla \qquad \text{with} \qquad \nabla = \begin{cases} \nabla_{rad} = \frac{3\kappa}{16\pi acG}\frac{lP}{mT^4} & \text{if } \nabla_{rad} \leq \nabla_{ad} \\ \nabla_{ad} + \Delta\nabla & \text{if } \nabla_{rad} > \nabla_{ad} \end{cases} \\
\frac{\partial X_i}{\partial t} &= \sum \pm X_i X_j \langle\sigma v\rangle_{ij} + \frac{\partial}{\partial m}\nabla\frac{\partial X_i}{\partial m}
\end{aligned}
$$

Each of the equations depends on all the others. With this set of coupled differential equations one is able to compute the evolution of stars with numerical methods if the boundary and initial conditions are given (Pols, 2009a).

Wolf-Rayet stars have very strong line driven winds which can reach velocities up to several thousand kilometers per second. Because of their high densities the winds of Wolf-Rayet stars are optically thick and their radius can not be observed directly. As a consequence of that one can not determine the temperature via the Stefan-Boltzmann law. Nevertheless it is possible to obtain their radii and with this their temperature by accurate spectral analysis of line-blanked atmospheric models which was done by Hamann et al. (2006).

In this thesis, the focus lies on massive helium stars of masses $M \gtrsim 7\,M_\odot$, which are represented in the galaxy by hydrogen-free Wolf-Rayet stars (WNE). The current problem is that the stellar models predict all helium stars to lie close to the helium zero-age-mainsequence (He-ZAMS) in the Hertzsprung-Russel diagram (HRD). However the estimated temperatures of the Wolf-Rayet (WR) stars do not accord with the model predictions that can be seen in Figure 1.

The winds of WR stars have a strong dependence on metallicity. Moreover the metallicity has effects on the mass-loss rate which depends on the velocity of the winds.

For the numerical solution only the mass of a star is used as initial parameter. This thesis will investigate if there is a dependence of the temperature on metallicity for hydrogen free WR stars and whether one has to take into account the metallicity as second initial parameter.

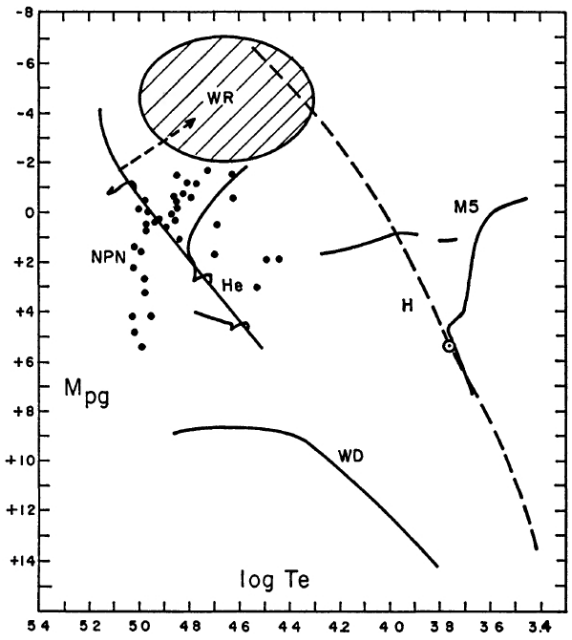


Figure 1: HRD with photometric magnitude $M_{pg}$ and the logarithmic temperature $log(T_e)$. The solid line labeled "He" represents the predicted helium mainsequence while the dashed circle represents the location of the WR stars. (Divine, 1965)

The temperatures of all WNE stars are adopted from Hamann et al. (2006). To obtain the present-day radial metallicity distribution, the published Gaia Data Release 2 (Gaia Collaboration et al., 2018) was used to estimate the distance to the sun and to the galactic center. All methods that have been used to determine the temperature, the distances as well as the radial metallicity gradient, the luminosity and the mass-loss rate are described in chapter 2. In chapter 3 the estimate of the present-day radial metallicity gradient, the improvements of luminosity and mass-loss rate resulting from the newly determined distances are presented and discussed. The question if the metallicity needs to be consider as second initial parameter for stellar models of WR stars will be answered. A summary of the results is given in chapter 4.

## 2 Methods

As previously mentioned, Wolf-Rayet stars have very strong line driven winds. This type of wind is related to the absorption and re-emission of photons that are created in the center of the star during nuclear fusion processes. The photons risen from nuclear burning processes in the core have high energies and are related to the ultra-violet (UV) band. As a consequence of this the resonance lines refer to C, N, O and elements of the Fe-group in the Lyman continuum (Lamers & Cassinelli, 1999a). To reach supersonic velocities of some thousand kilometers per second each ion has to absorb $10^4 - 10^7$ photons per second. It follows that only transitions with short lifetimes ($\tau \simeq 10^{-7}\,\mathrm{s}$) are relevant for the radial acceleration to these high velocities (Lamers & Cassinelli, 1999a).

Wolf-Rayet stars have strong emission lines which result from the high velocity and density of the winds. For the same reason the probability that ions and electrons recombine is high. This leads to excited electrons which emit light every time electrons return to a lower energy level. In the spectra of Wolf-Rayet stars very high excited energy levels can be observed. The emission lines of different elements seen in their spectra define the evolutionary stage and the subtype of the Wolf-Rayet star.

WR stars with hydrogen present in their surface abundances which also show emission lines of helium and nitrogen are called WNL stars. WNE stars are similar in terms of their helium and nitrogen abundances to WNL stars apart from their lack of hydrogen. WC stars show almost no nitrogen in their spectrum but have strong carbon emission lines. The last type, the WO stars, are similar to WC stars but have strongly increased oxygen lines (Pols, 2009b).

As a consequence of the strong emission lines and the high wind velocities, the observer of a Wolf-Rayet star will see almost no absorption lines in the spectra represented by a P Cygni profile for the UV resonant lines. A schematic illustration of the sections that characterize such a profile are shown in Figure 2.

The star emits a continuous spectrum but the photons with the energies of the resonance lines will be scattered in all directions, when they are re-emitted by the ions. This has different effects in each region of the wind. In the tube 'F' only a small fraction of the photons will be scattered in the direction of the observer, such that an absorption is seen. The wind pointing towards the observer leads to a Doppler broadening of the absorption in the range of $-v_\infty$ to $0$. The tube 'O' can not be seen by the observer because it is shielded by the star. As a consequence of this one can not see absorption lines that are red-shifted in the range of $0$ to $v_\infty$. The halo 'H' scatters radiation which is seen by the observer as emission lines. They are Doppler shifted between $-v_\infty$ and $v_\infty$. The P Cygni profile is the sum over these effects, visualized on the right of Figure 2 (Lamers & Cassinelli, 1999b).

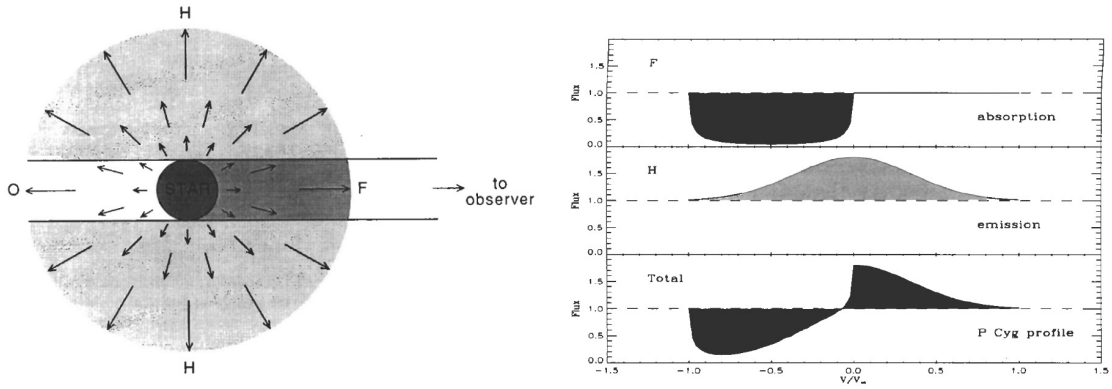


Figure 2: Left: Schematic illustration of a stellar wind with outward increasing velocity. There are four regions: The star in the center, the tube pointing to the observer 'F', the tube shielded by the star 'O' and the halo 'H' surrounding the star. Right: The emission and absorption lines of F and H and the sum of both over the continuous spectrum of the star. (Lamers & Cassinelli, 1999b)

As already mentioned the winds are optically thick and one can not observe the star directly. The homogeneous star lies deep within the wind. To derive its properties via line-blanketed atmospheric models, one has to adopt an optical depth $\tau$. The optical depth defines where the homogeneous star ends and the wind starts. In this thesis this is defined to be at the point where the wind velocity gets supersonic. For normal O-type stars one might apply an Rosseland optical depth of $\tau = 2/3$, while for Wolf-Rayet stars previous studies suggest that the optical depth of $\tau = 20$ to be more representative (Crowther, 2007). These differences are visualized in Figure 3.

To determine the temperature of a star the Stefan-Boltzmann law, equation 1, is used.

$$L = 4\pi\sigma R^2 \mathrm{T}^4 \tag{1}$$

Because the radius $R$ of a Wolf-Rayet star can not be measured, the stellar radius $R_*$ at an optical depth of $\tau = 20$ is used to determine the stellar temperature $\mathrm{T}_*$.

The classical mass-loss rate of a Wolf-Rayet star can not be determined. Still it is possible to get an mass-loss rate from the spectrum of a star which is independent from luminosity. This is called transformed mass-loss rate $\dot{M}_t$.

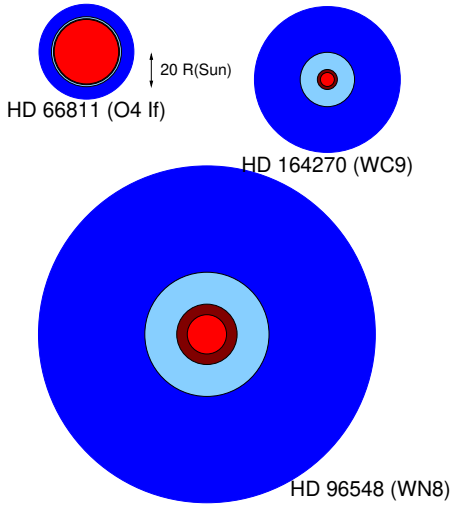


Figure 3: Comparison of the optical depth of $\tau = 20$ (red) and $\tau = 2/3$ (dark-red). In dark-blue the primary optical wind line-forming region is illustrated, while the higher density wind material is colored in light-blue, showing the highly extended wind of Wolf-Rayet stars. (Crowther, 2007)

## 2.1 Stellar temperature $T_*$

The Potsdam group of Hamann et al. (2006) made precise line-blanked atmospheric models for all WNE and WNL stars without a companion star. In the present work the focus lies on the galactic WNE stars so only data corresponding to these will be used. In their paper the Potsdam group made a huge grid of different atmospheric models to cover the range of all Wolf-Rayet stars and luminosities. These models are current state of the art and in this work the gained temperatures will be adopted. The gridspacing between each estimated temperature is $\pm \log(0.05)$ which will be adopted as uncertainty for each temperature.

## 2.2 Present-day radial metallicity gradient

To find out if the metallicity is a second initial parameter, one needs to derive the present-day radial metallicity gradient. In the bulge of the galaxy one predicts a metallicity that is higher than the solar metallicity. This is caused by the higher population of stars which feed the interstellar medium with Fe-group elements after their explosion leading to an increase of metallicity in the bulge. In the outer regions of the galaxy one expects the metallicity to be lower than the solar one, as the population density is lower.

To inspect the radial metallicity distribution, one has to focus on young stars $\leq 2\,\mathrm{Gyr}$'s, because high mass stars produce Fe-group elements during further nuclear burning processes. This influences the $[Fe/H]$ ratio and with this the metallicity. The dependence of the age of a star on its metallicity has been discussed by Anders et al. (2017b), who discovered that the deviations of the current metallicity increases rapidly within the first $10\,\mathrm{Gyr}$'s. In Figure 4 it is

clear to see that the galactic distribution of the $[Fe/H]$ ratio changes fast. Already after 2 Gyr's the ratio is further distributed and no longer on a straight line.

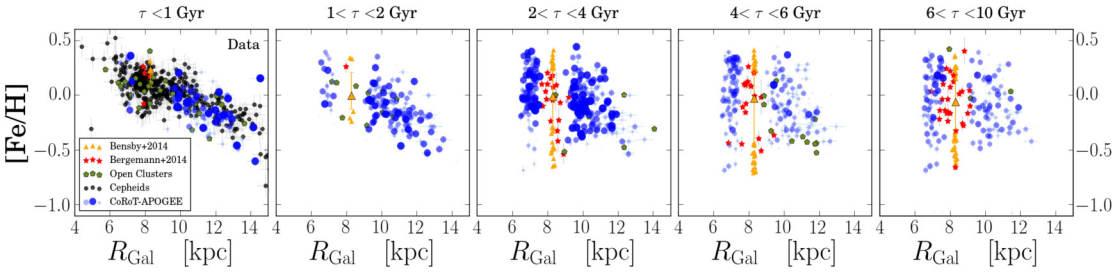


Figure 4: The $[Fe/H]$ vs. $R_{\text{gal}}$ distribution close to the galactic plane $\left(|z_{\text{gal}}| < 0.3\,\text{kpc}\right)$ for five different ages. The Red Giants observed by CoRoT and APOGEE (Anders et al., 2017a) are shown in blue, the open clusters compilations of Genovali et al. (2014) and Magrini & Randich (2015) in green, the subgiant sample from Bergemann, M. et al. (2014) in red, the galactic Cepheids from Genovali et al. (2014) in black and the Solar Neighborhood FGK dwarf sample of Bensby et al. (2014) in orange. (Anders et al., 2017b)

There are diverse methods to determine the metallicity from different element ratios. In this work the $[Fe/H]$ ratio has been chosen to estimate the metallicity $Z$. To approximate the metallicity from this ratio the following equation is used

$$\begin{aligned} [Fe/H] &= \log\left(Z/Z_{\odot}\right) - \log\left(X/X_{\odot}\right) \\ [Fe/H] &\approx \log\left(Z/Z_{\odot}\right) \qquad \text{assuming} \quad X \simeq X_{\odot} \end{aligned} \tag{2}$$

Here the hydrogen abundances are approximated to remain almost constant throughout the galaxy (Bertelli et al., 1994).

To cover a large area of the galaxy young open cluster, the Cepheids and field member stars of previous studies are taken into account. All these studies are made with different observations and methods of analysis to determine the $[Fe/H]$ ratio. Unfortunately the different observations lead to a variation in the systematic uncertainty. Nevertheless the uncertainties of the observations themselves are much bigger than the systematic uncertainty. More than 540 stars have been taken into account to reduce the inaccuracy of the uncertainties.

## 2.3 Distances

To obtain the individual initial metallicity of each Wolf-Rayet star the distance of the star to the sun needs to be known. With this information one can compute the distance of the star to the

galactic center. In the following the previous distance estimates of van der Hucht (2001) and Hamann et al. (2006) are introduced. Moreover, the methods of obtaining the distances given in this thesis by the Gaia Data Release 2 (Gaia Collaboration et al., 2018) and how these can be improved by proper motion corrections of Bailer-Jones et al. (2018) will be discussed.

### 2.3.1 Previous estimates

For the VII'th catalogue of galactic Wolf-Rayet stars of van der Hucht (2001), 227 Wolf-Rayet stars are listed of which 127 are WNE or WNL stars. To estimate the distance of star to the sun intrinsic colors, color excesses and absolute magnitudes were used to obtain the photometric distances. Moreover open clusters and OB associations distances were considered to conclude the distance ot the stars. For some individual stars the distance was estimated by approximated parallaxes. The average uncertainty of these determinations is about $50\,\%$ for Wolf-Rayet field stars, for individual stars the uncertainty can exceed a factor of $2.5$.

In the paper of Hamann et al. (2006) similar methods were used to determine the distances of the Wolf-Rayet stars to the sun. Some distances are adopted from the VII'th van der Hucht (2001) catalogue. No uncertainties are given by Hamann et al. (2006). The distance to the sun is listed as distance modulus $DM$. To re-calculate the distance $d$ in kilo parsec from this parameter one has to use the following formula (Schneider, 2004).

$$d = 10^{1+\frac{DM}{5}} \tag{3}$$

The differences and improvements of these two estimates will be discussed in chapter 3.

### 2.3.2 Gaia Data Release 2

In 2018 the Gaia Collaboration et al. (2018) published the Gaia Data Release 2. The Gaia satellite took data from around 1.7 billion stars in our galaxy and measured the position, parallax and proper motion of over 1.3 billion stars. The uncertainty of the measured parallax and position is given roughly by $0.02 - 0.04\,\mathrm{mas}$ (Gaia Collaboration et al., 2018) which results in an uncertainty of approximately $10\,\%$.

Estimating the distance from a parallax is a non-trivial issue as the transformation is nonlinear and the distance is always defined positive. This is discussed by Bailer-Jones et al. (2018) who solve the problem by taking the longitude and latitude into account, which leads to an upper and lower limit. They also consider the proper motion of each star which allows to estimate the distances from parallax in an improved way.

To access these corrections one has to visit http://gaia.ari.uni-heidelberg.de/tap.html and choose the table 'geometric_distances' within the scheme 'gaiadr2_completements'. To obtain the data

following commands were used:

```
SELECT DISTANCE(POINT('ICRS',ra,dec),POINT('ICRS',raj2000,dej2000))
AS dist,source_id, ra, dec, phot_g_mean_mag, r_est, r_lo, r_hi
FROM twomass
JOIN gaiadr2.gaia_source ON 1=CONTAINS(POINT('ICRS',ra,dec),
CIRCLE('ICRS',raj2000,dej2000,0.00027777))
JOIN gaiadr2_complements.geometric_distance USING (source_id)
WHERE mainid = 'XXX+XXX'
ORDER BY dist
```

The code searches in the 2MASS table for the right ascension and declination of the examined star. Then a cross relation to the table published within the Gaia Data Release 2 is made and linked to the table containing the corrected distances. The table calculates a circle of 1 arc second around the right ascension and declination of the 2MASS data and checks for all stars within this range in the Gaia Data Release 2. The output consists of the distance, solution identifier, right ascension and declination of the star as well as the estimated distance from the sun. The input 'XXX+XXX' is the 2MASS identification number.

To verify that the output of the table contains the star of interest the galactic latitude and longitude were compared with data of previous works that are listed on Simbad. Another method to confirm the results is to check whether the mean G-Band magnitude matches with determinations of the data on Simbad. If there is no G-Band magnitude available in Simbad the magnitude is requested to lie near the V-Band and over the J-Band.

### 2.3.3 Galactic distances

All distances that were estimated previously in this work are the distances of the stars to the sun. To obtain the metallicity from the radial metallicity gradient one needs to know the distance $R_{\text{gal}}$ of the star to the galactic center. For further calculations the distance of the sun to the galactic center is set to $(8.0 \pm 0.5)\,\text{kpc}$. Simple geometric considerations show that the galactic radius of each star is given by

$$R_{\text{gal}} = \sqrt{d^2 + 64\,\text{kpc}^2 + 16\,\text{kpc} \cdot d\cos(l)\cos(b)} \tag{4}$$

where $d$ represents the distance to the sun in kilo parsec, $b$ the galactic latitude and $l$ the galactic longitude (van der Hucht, 2001).

## 2.4 Corrections

As already mentioned the newly estimated distances are more accurate than previous estimates. These improvements lead to corrections of previously estimated values that depend on the distance to the sun. This includes the luminosity, mass and mass-loss rate.

### 2.4.1 Luminosity

The luminosity is the only parameter that depends directly on the distance ($L \propto d^2$). Knowing the previous luminosity and distance which are adopted from Hamann et al. (2006) one can simply calculate the corrected luminosity.

$$L = \frac{L_{\text{prev}} d^2}{d^2_{\text{prev}}} \tag{5}$$

The index 'prev' indicates the values adopted in previous works. Parameters without indices represent the corrections.

### 2.4.2 Mass

The mass of a star which should be taken as first initial parameter follows a mass-luminosity relation. In the study from Gräfener et al. (2011), a mass-luminosity relation has been derived as an analytical expression for chemical homogeneous stars. To achieve this grids within different mass ranges for hydrogen and helium stars were computed. The helium star beneath the wind can be seen as homogenous and therefore can be described by the mass-luminosity relation. The WR stars of interest are expected to lie in a mass range of $M = 5 - 40\,\mathrm{M}_\odot$. To cover this range the grid in the range of $0.6 - 100\,\mathrm{M}_\odot$ is used.

$$\log\left(M/M_\odot\right) = 3.059 - \sqrt{14.76 - 2.049\log\left(L/L_\odot\right)} \tag{6}$$

### 2.4.3 Mass-loss rate

In the paper of Hamann et al. (2006) only the transformed mass-loss rate is given. To correct this value one firstly has to calculate the mass-loss rate of the star with the previously estimated parameters. The new value for the transformed mass-loss rate can be determined by using the mass-loss rate and newly estimated luminosity.

$$\log\left(\frac{\dot{M}_{\mathrm{t}}}{M_{\odot}yr^{-1}}\right) = \log\left(\frac{\dot{M}}{M_{\odot}yr^{-1}}\right) - 0.5\log\left(f\right) - \log\left(\frac{v_{\infty}}{1000\,\mathrm{kms}^{-1}}\right) - 0.75\log\left(\frac{L}{10^{6}L_{\odot}}\right) \tag{7}$$

In this equation $\dot{M}_{\mathrm{t}}$ is the transformed mass-loss rate, $\dot{M}$ the mass-loss rate, $f = \frac{1}{D}$ the inverse clumping-factor, $v_{\infty}$ the stellar wind velocity and, last but not least, $L$ as the luminosity (Bestenlehner et al., 2014). In Hamann et al. (2006) a clumping-factor of $D = 4$ is used. For further calculations in this thesis $D = 1$ will be used since it only causes a linear shift for all mass-loss rates. Current works approximate the clumping-factor by $D = 10$ which might change again in future works. Using a clumping-factor of $D = 1$ keeps the obtained results independent from this factor.

# 3 Analysis

In this chapter the results of this work are presented. At first the present-day radial metallicity gradient of our galaxy will be discussed. Next the newly determined distances of the hydrogen free Wolf-Rayet stars are compared to previous results. Then the newly determined luminosities and masses are compared to previous estimates and the mass-loss rate, which is predicted to depend on metallicity, will be analyzed. At last the estimates of metallicity, mass and temperature are analyzed with respect to the metallicity as second initial parameter.

## 3.1 Present-day radial metallicity gradient

For the estimate of the present-day radial metallicity gradient, it is important that it covers a wide range of the galaxy. As a consequence, the set of data contains about 540 stars which are spread over the range of $4 - 18\,\mathrm{kpc}$. In this analysis the metallicity is assumed to be distributed evenly throughout the separation of the galactic plane $z_{\mathrm{gal}}$, thus that it is a function of the galactic radius $R_{\mathrm{gal}}$.

The set of data contains different types of young stars. Cepheids, young field stars and stars of different clusters were used. It is important that these stars are younger than $2\,\mathrm{Gyr}$'s to be representative for the Wolf-Rayet stars. Another criterion is that the stars do not lie in the same region of the galaxy. So the location of the clusters and individual stars were checked to guarantee that the gradient only depends on the radial parts.

Figure 5 shows the present-day radial metallicity distribution. The uncertainties in the graph are omitted for the sake of better visualization. The $[Fe/H]$ abundance is a linear function of the galactic radius. It is clear to see that there are high fluctuations in the $[Fe/H]$ abundance, caused by the observational methods that have been used in the previous works. From linear regression one obtains for the $[Fe/H]$ abundance

$$[Fe/H]\,(R_{\mathrm{gal}}) = (-0.047 \pm 0.003)\,\mathrm{kpc}^{-1} \cdot R_{\mathrm{gal}} + (0.431 \pm 0.024) \tag{8}$$

with a reduced Chi-square of $\chi^2_{\mathrm{red}} = 0.024$, which is very small caused by the fluctuations in the $[Fe/H]$ abundance. Since the degree of freedom is pretty high with $df = 532$ one may accept higher deviations of the reduced Chi-squared. It might be possible to increase Chi-squared by averaging over the individual clusters.

Comparing this result to the previous works of Genovali et al. (2014) and Magrini & Randich (2015) one finds out, that the obtained slope remains almost the same. This confirms the assumption of a linear dependence and allows us to calculate the metallicity of each star via formula 2.

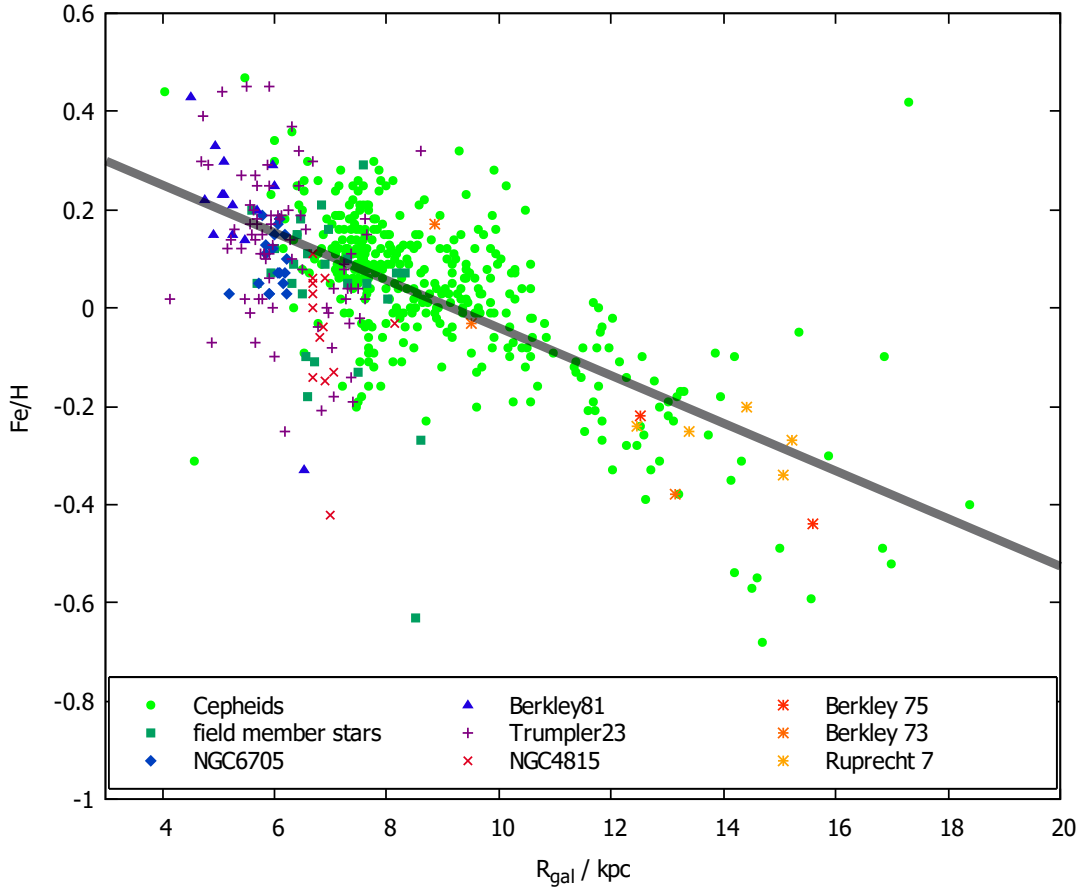


Figure 5: The light-green circles are galactic Cepheids adopted from Genovali et al. (2014), the green squares represent young field stars from Magrini et al. (2017). The blue diamonds are members of the NGC6705 cluster from Cantat-Gaudin et al. (2014) while the blue triangles of Berkley 81 are adopted from Magrini & Randich (2015), the purple crosses of Trumpler 23 from Overbeek et al. (2017) and the red x's of cluster NGC4815 from Friel et al. (2014). The red, orange and yellow triple-crosses are Berkley 75, 73 and Ruprecht 7, respectively, and taken from Carraro et al. (2007). The black line is a linear regression to obtain the $[Fe/H]$ abundance as function of the galactic radius $R_{\rm gal}$.

## 3.2 Distances

As introduced in the previous chapter distance only have been approximated by cluster assumptions for a long time. Now that the Gaia DR2 archive is accessible one can figure out the distances to the sun of almost all hydrogen-free Wolf-Rayet stars. The results are listed in Table 1 of the appendix. Unfortunately WR2 and WR63 have no measured parallax, thus that no correction could be applied in these cases.

Figure 7 shows the location of each WNE star in our galaxy derived from 3 different sources. One can clearly see improvements with each picture furthermore the position of most stars correspond to their estimated location. For example WR1 is always located near the Perseus Arm. Nevertheless there are outliers like WR107 which have high fluctuation in their distance estimates. This difficulty in determining the distances reflects in higher uncertainties.

It is clear to see that the positions estimated with the Gaia Data Release 2 are higher concentrated on the spiral arms of our galaxy. For the previous estimated locations one can see that some stars lie in gaps between the spiral arms. Major improvements can be seen in the Carina spiral arm on the right side of the sun. There the Wolf-Rayet stars seem to be distributed equally, while in previous estimates that these stars are related to clusters with known distance.

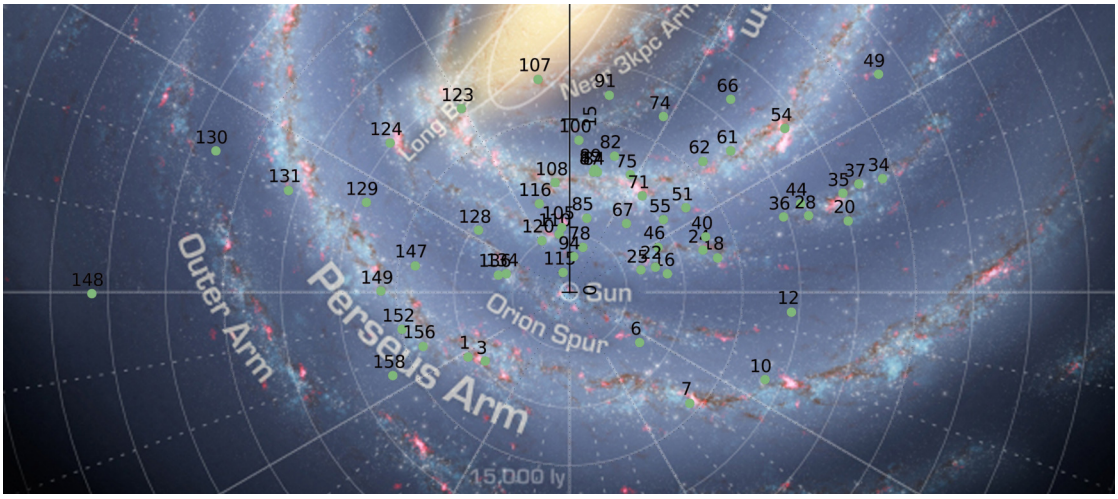


Figure 6: All WN stars without companion star and their galactic location adopted from Bailer-Jones et al. (2018). The map is taken from the official NASA website. (NASA, 2017)

Figure 6 shows all WNE and WNL stars without companion star at their location in our galaxy estimated with the Gaia Data Release 2. Again one can see that almost all stars lie on spiral arms.

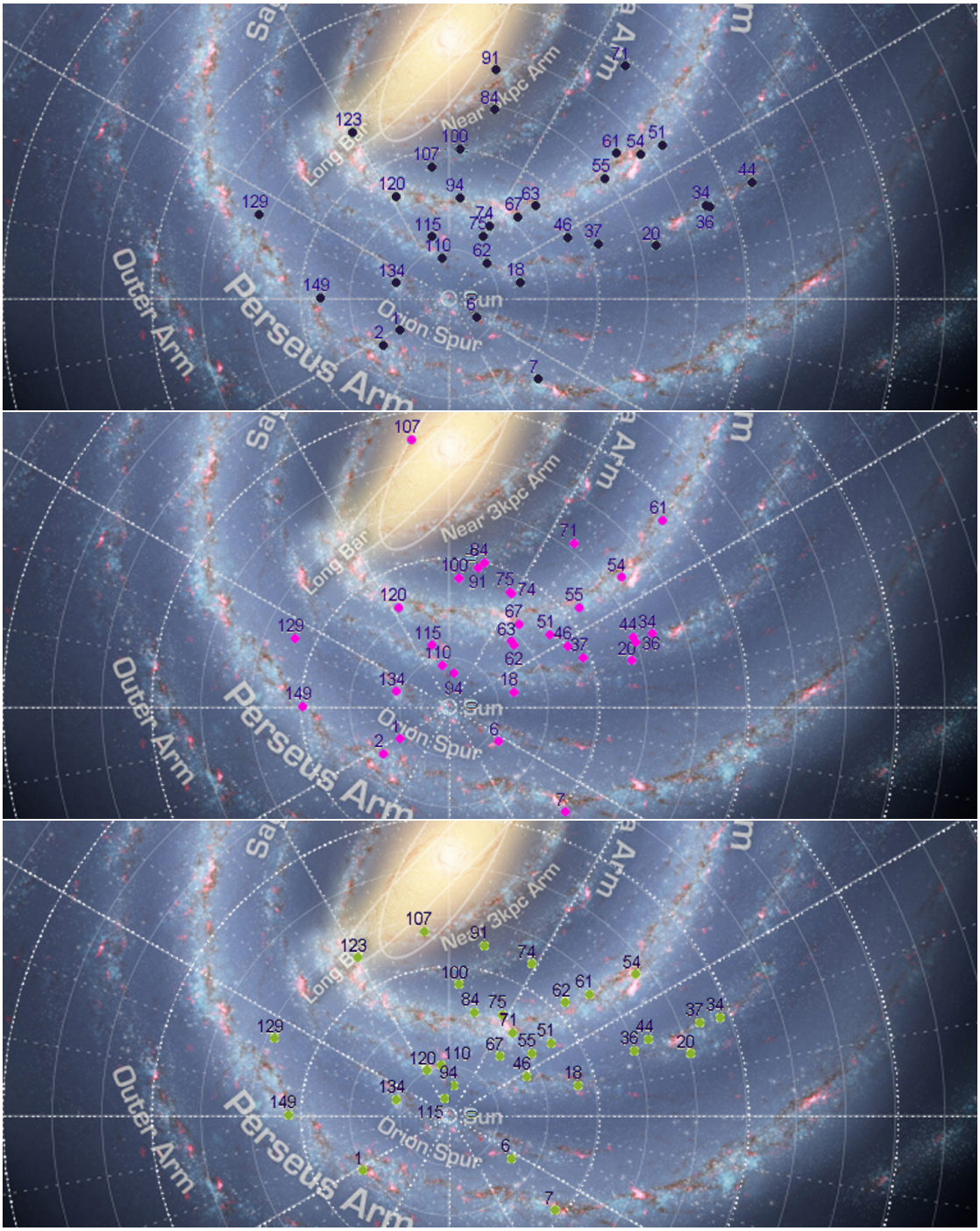


Figure 7: Top: WNE stars and their galactic location adopted from van der Hucht (2001); Middle: WNE stars and their galactic location adopted from Hamann et al. (2006); Bottom: WNE stars and their galactic location adopted from Bailer-Jones et al. (2018); The map is taken from the official NASA website. (NASA, 2017)

## 3.3 Luminosity

The improved distance estimates lead to corrections of the derived luminosities which are adopted from Hamann et al. (2006). The uncertainty of luminosity is given in form of a higher and lower bound resulting from the distance estimates, which represent an approximation about the order of inaccuracy. The newly determined luminosities for the WNE and WNL stars are listed in Table 2 and 3 in the appendix.

Figure 8 shows the HRD derived by Hamann et al. (2006) on the left and on the right side the HRD with corrected luminosities. Both HRD's have been scaled to equal size to make comparison easier. One can observe that hotter WNE stars got brighter while the luminosity for cooler stars declines. Moreover all WNE stars lie on the left side of the hydrogen ZAMS line. In this diagram the WNL stars are shown too. Inspecting both the WNE and WNL stars one derives that the fluctuations in luminosity are much higher than before, leading to a widened band in luminosity.

Figure 9 shows the HRD for WNE stars with their uncertainties. The uncertainties in temperature is given by $\Delta \mathrm{T}_* = \pm \log(0.05)$, the step width in the gridspace. Stars of the same temperature are shifted so that the individual uncertainties are visible. Having a look at the different WNE stars, it is clear to see that some stars have relatively small uncertainties while WR107 and WR115 have very big uncertainties. As already discussed in the previous chapter this is caused by problems in the estimation of the distance. These stars have to be handled with care. Especially WR115 seems to have a very low luminosity. Another interesting fact is that the uncertainties in luminosity seem to get bigger for lower temperatures.

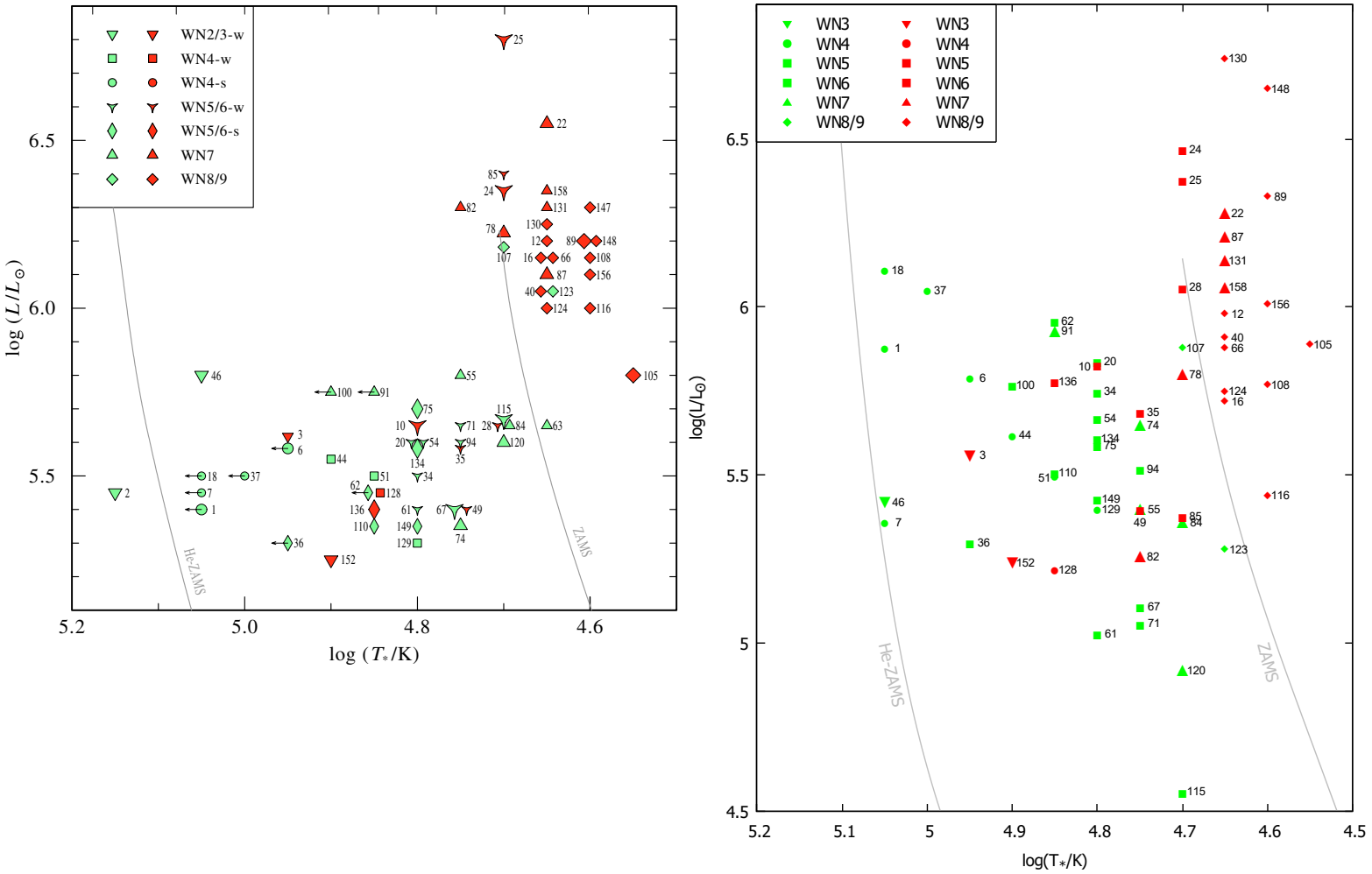


Figure 8: Left: HRD from Hamann et al. (2006), the arrows indicate that these stars may be hotter, caused by parameter degeneracy. Right: HRD with corrected luminosities, but the same temperature. The ZAMS lines in the right panel have been estimated using MESA. The red symbols indicate Wolf-Rayet stars with hydrogen and green symbols those without any.

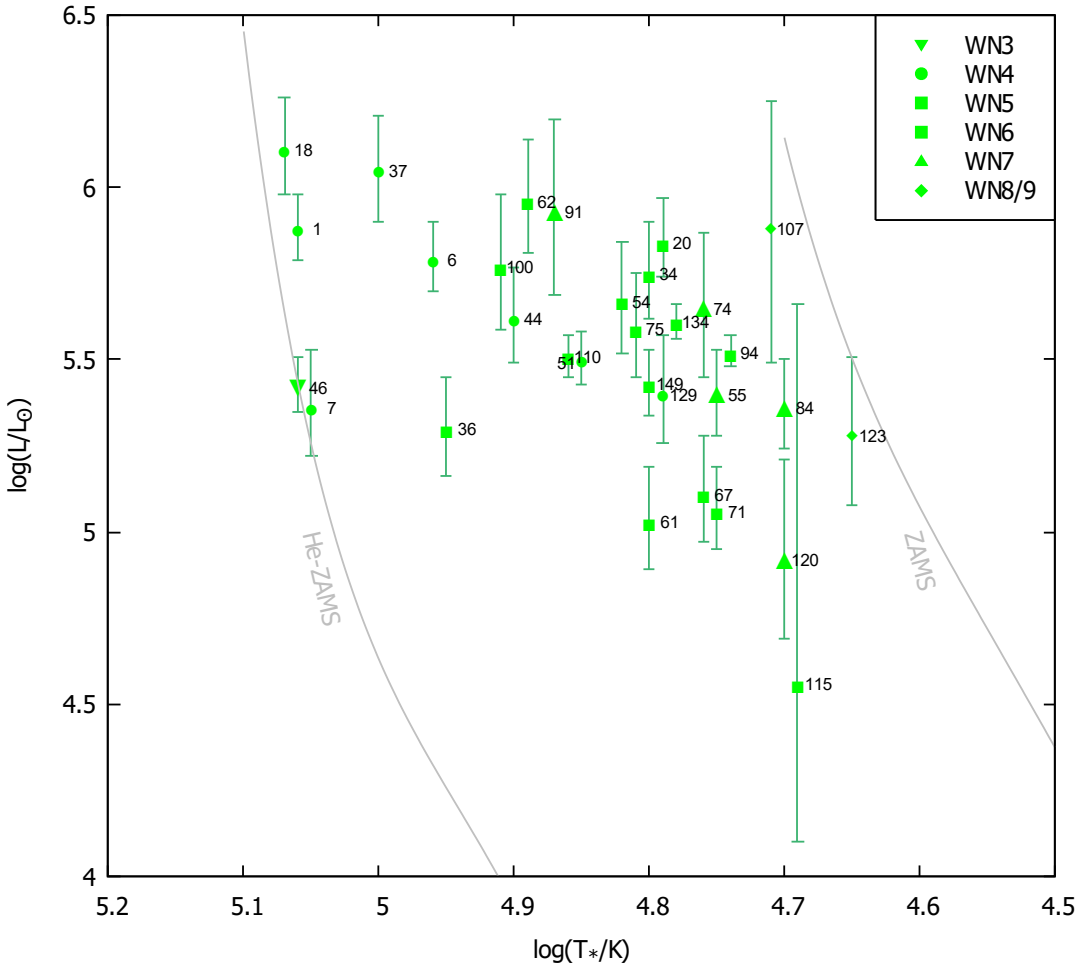


Figure 9: HR-diagram with corrected luminosities and errorbars for WNE stars. The different symbols indicate to which spectral subtype the individual star belongs to.

### 3.4 Mass-loss rate

For Wolf-Rayet stars, which have high mass-loss rates one expects a correlation between mass-loss rate and luminosity. An example for this relation for hydrogen free WN stars is given by Tramper et al. (2016) describing the proportionality of the mass-loss rate to the luminosity. They found out that the mass-loss rate scales with

$$\log\left(\frac{\dot{M}}{M_\odot yr^{-1}}\right) = (-9.30 \pm 0.35) + (0.85 \pm 0.06)\log\left(\frac{L}{L_\odot}\right) + (0.44 \pm 0.08)Y + (1.3 \pm 0.2)\log\left(\frac{Z}{Z_\odot}\right)$$

Figure 11 shows the mass-loss luminosity relation for WNE stars assuming that all stars have the same metallicity. On the left side the relation derived by Hamann et al. (2006) is shown and on the right the newly determined luminosities and mass-loss rates of the WNE stars. It is clear to see that in the left diagram the scatter of the WNE stars is relatively high, while in the right diagram the scatter is drastically reduced and one can see a linear relation. Applying a linear regression on the set of data returns for the mass-loss rate as function of luminosity:

$$\log\left(\frac{\dot{M}}{M_\odot yr^{-1}}\right) = (-9.06 \pm 0.80) + (0.87 \pm 0.14)\log\left(\frac{L}{L_\odot}\right)$$

Comparing this to the results of Tramper et al. (2016) both mostly agree with each other. However keeping in mind that a clumping factor of $D = 1$ has been chosen as offset. Applying another clumping factor would cause a linear shift in the offset. The reduced Chi-squared is relatively small with $\chi^2_{\text{red}} = 0.077$. The degree of freedom is given by $df = 29$. The small reduced Chi-squared could be caused by the fact that the uncertainties only depend on the uncertainties of the distance estimates.

Taking the metallicity into account it is suspected that the mass-loss rate scales with a factor of $\dot{M} \propto Z^{\frac{1-\alpha}{\alpha}}$ (Puls et al., 2008). Figure 10 shows the mass-loss rate over the luminosity as function of the metallicity to determine the factor $\frac{1-\alpha}{\alpha}$. For the luminosity an exponent of $0.87$ had been chosen as it fits the expectations. The offset is left open because the uncertainty is relatively high. One then obtains

$$\log\left(\frac{\dot{M}}{M_\odot yr^{-1}}\left(\frac{L}{L_\odot}\right)^{-0.87}\right) = (-9.16 \pm 0.06) + (0.80 \pm 0.47)\log\left(\frac{Z}{Z_\odot}\right)$$

It is clear to see that the uncertainty of the metallicity is very high due to the large scatter. A linear relation can only be guessed. These fluctuations are reflected in the reduced Chi-squared with $\chi^2_{\text{red}} = 0.068$ and the degree of freedom $df = 29$. Nevertheless this confirms the assumption that the mass-loss rates of WNE stars have a strong dependence on the luminosity

and somewhat weaker on the metallicity as it has been discussed earlier in Nugis & Lamers (2000).

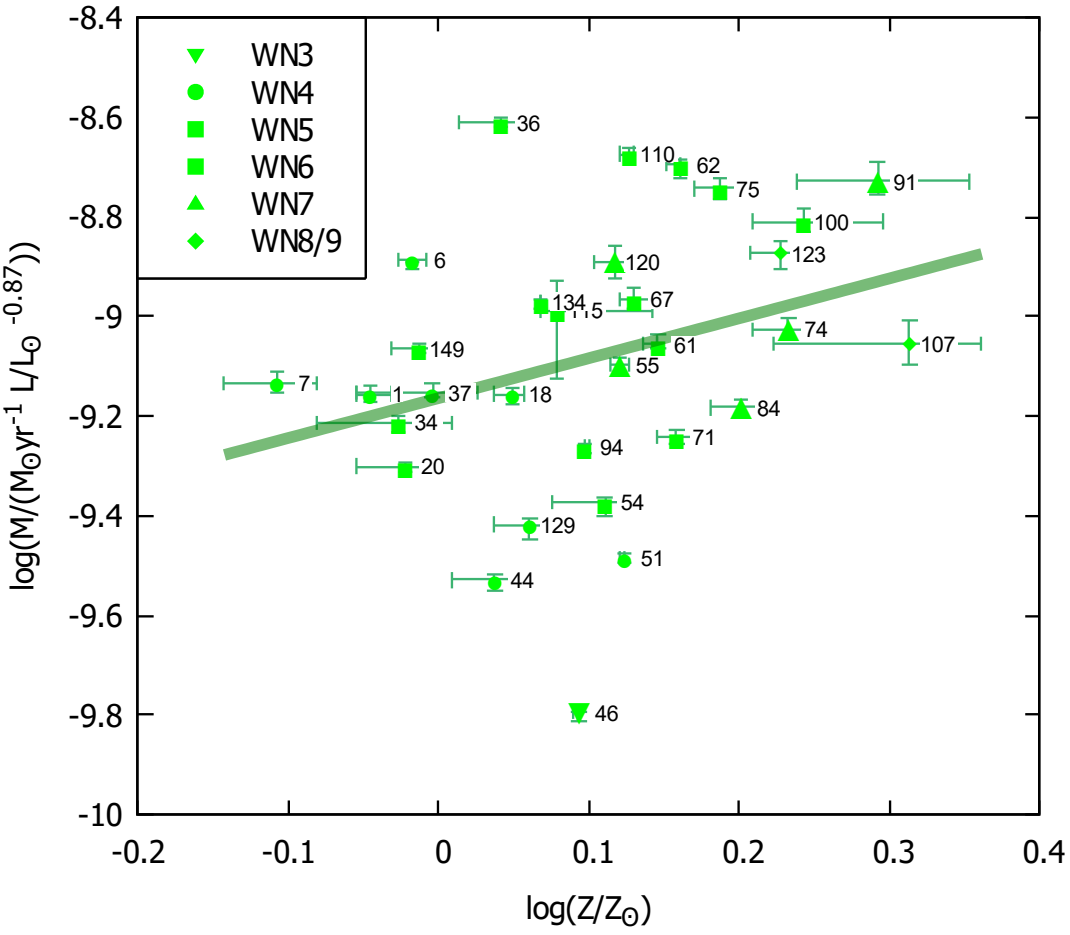


Figure 10: Mass-loss over luminosity versus metallicity for WNE stars. The individual green point types represent the different spectral subtypes of the WNE stars.

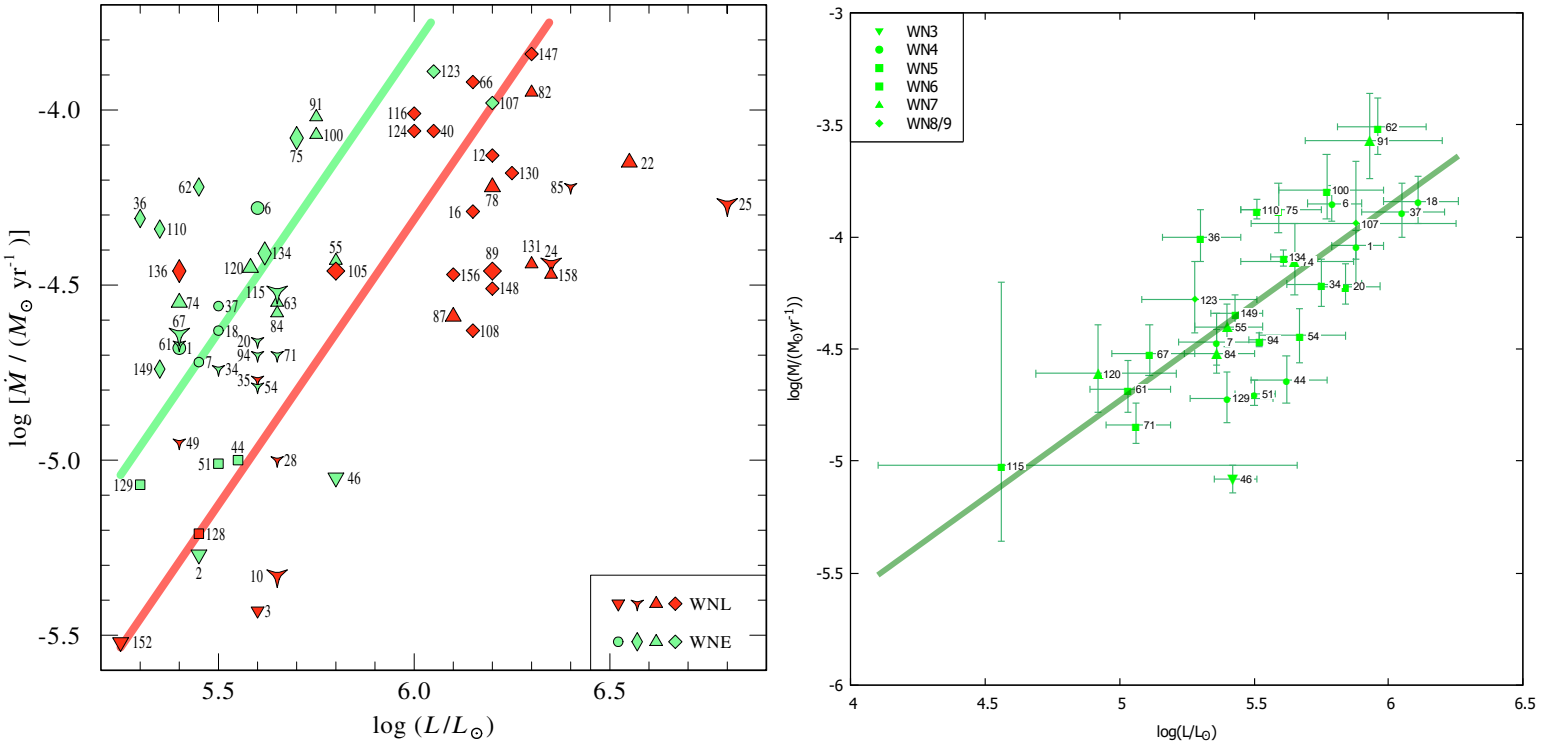


Figure 11: Left: Mass-loss luminosity relation from Hamann et al. (2006). The WNE stars are shown in green, separated by spectral subtypes like before and WNL stars are illustrated in red with the same notification. Right: The mass-loss luminosity relation with the newly determined luminosities and mass-loss rates for WNE stars separated for different spectral subtypes.

### 3.5 Metallicity as second initial parameter

For stellar models of stars in our galaxy only one initial parameter, the mass of a star, and the stellar structure equations are needed. This is true for all hydrogen burning stars. Moreover the calculated models of massive helium stars do not fit to the observation of the WNE stars. For these stars parameters like the mass-loss have a strong dependence on the metallicity. It may be possible that the temperature too depends on the metallicity. Although for the stars of interest the estimated radial metallicity gradient changes only by a factor of 2 it might be interesting to investigate its influence on the stellar temperature.

It is clear that there is a relation between mass and temperature. To investigate if the metallicity can be seen as second initial parameter, a three dimensional graph is created. It contains the temperature, mass and metallicity. All stars are expected to lie on a plane. Figure 13 shows the result for the WNE stars, containing an adjustment plane that links all three parameters. The estimated temperatures, masses and metallicities of all WNE stars are listed in Table 5 of the appendix.

From the adjustment plane the temperature as a function of mass and metallicity is derived.

$$\log\left(\frac{\mathrm{T}_*}{K}\right) = (-0.59 \pm 0.15)\log\left(\frac{Z}{Z_\odot}\right) + (0.27 \pm 0.08)\log\left(\frac{M}{M_\odot}\right) + (4.57 \pm 0.10)$$

The Chi-squared test returns a reduced Chi-squared of $\chi^2_{\mathrm{red}} = 0.21$ and a degree of freedom of $df = 28$. Compared to previous approaches and considering that the uncertainties are only approximated, this result is quite good.

Figure 12 is a projection of the three dimensional graph in the $\log(\mathrm{T}_*)$-$Z$ plane. The pink diamonds represent stars of $(9 \pm 1)\,\mathrm{M}_\odot$, the red circles stars of $(14 \pm 2)\,\mathrm{M}_\odot$, the blue squares these with $(18 \pm 1)\,\mathrm{M}_\odot$ and the yellow triangles those one with $(28 \pm 2)\,\mathrm{M}_\odot$. The adjustment plane is shown for different masses and colored to the corresponding mass range. It is clear to see that most of the stars lie near or on the line within their uncertainties.

There are some outliers that are far off the plane. Reasons for their deviation from their expected position in the graph might be indicators in their spectra for an unknown companion star or predictions that these stars might actually be hotter. The five most drastic outliers are, in descending order, WR46, WR7, WR20, WR100 and WR36. WR46 contains some absorption lines in its spectrum and is supposed to have an OB companion star (Hamann et al., 2006), which could be a reason why WR46 lies so far apart from the expected plane. If the star has a companion star the mass would have been determined incorrectly. WR7, WR100 and WR36 were already supposed to be hotter and are sorted to the wrong temperature due to parameter degeneracy (Hamann et al., 2006). Only WR20 has no suspicious trades in its spectrum.

Nevertheless all this has to be handled with care, because the spectral analysis models depend

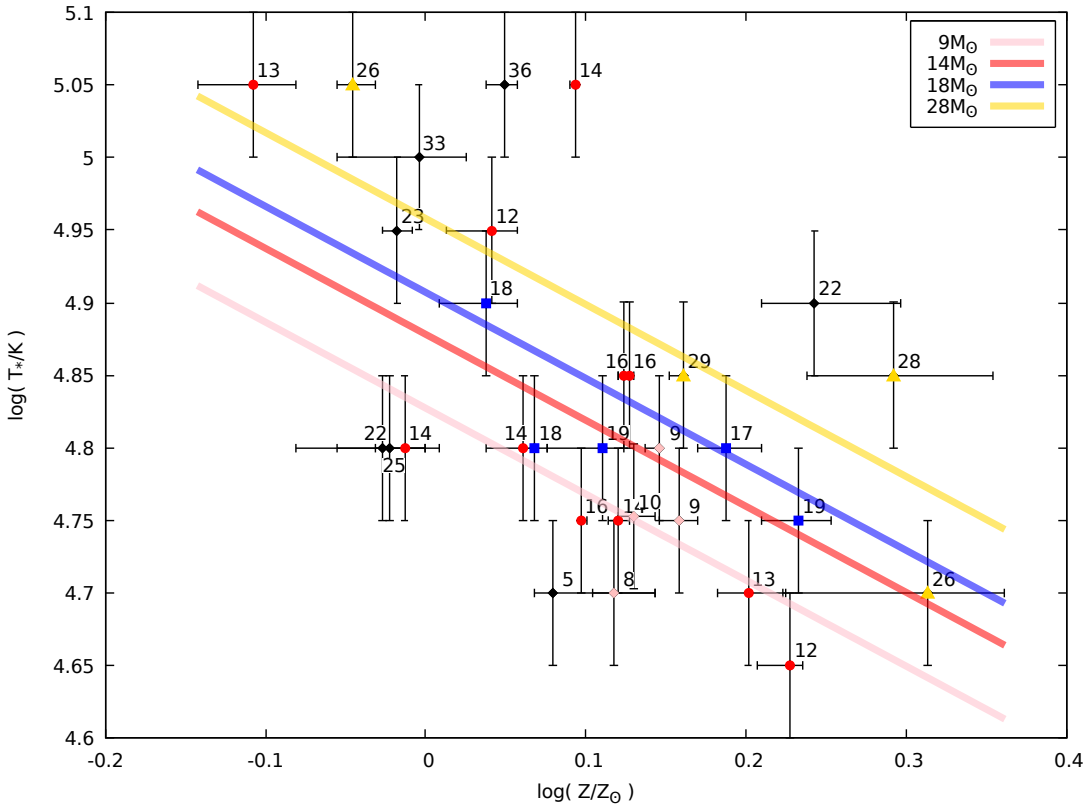


Figure 12: Temperature $T_*$ versus metallicity $Z$. The pink diamonds include stars of masses $(9 \pm 1)\,M_\odot$, the red circles stars with $(14 \pm 2)\,M_\odot$, the blue squares stars with $(18 \pm 1)\,M_\odot$ and the yellow triangles stars with $(28 \pm 2)\,M_\odot$. The grid is shown with the multicolored lines for given masses. The black diamonds represent all other stars that do not fit in the mass-ranges above.

on the metallicity and luminosity of a star which were recalculated during this work. This leads to unknown uncertainties in the temperature. Although, the result of this analysis is no evidence that there is a metallicity dependence on the temperature, it shows that there is some relation between the stellar temperature and the metallicity. In conclusion the metallicity may be taken into account as second initial parameter for stellar Wolf-Rayet models.

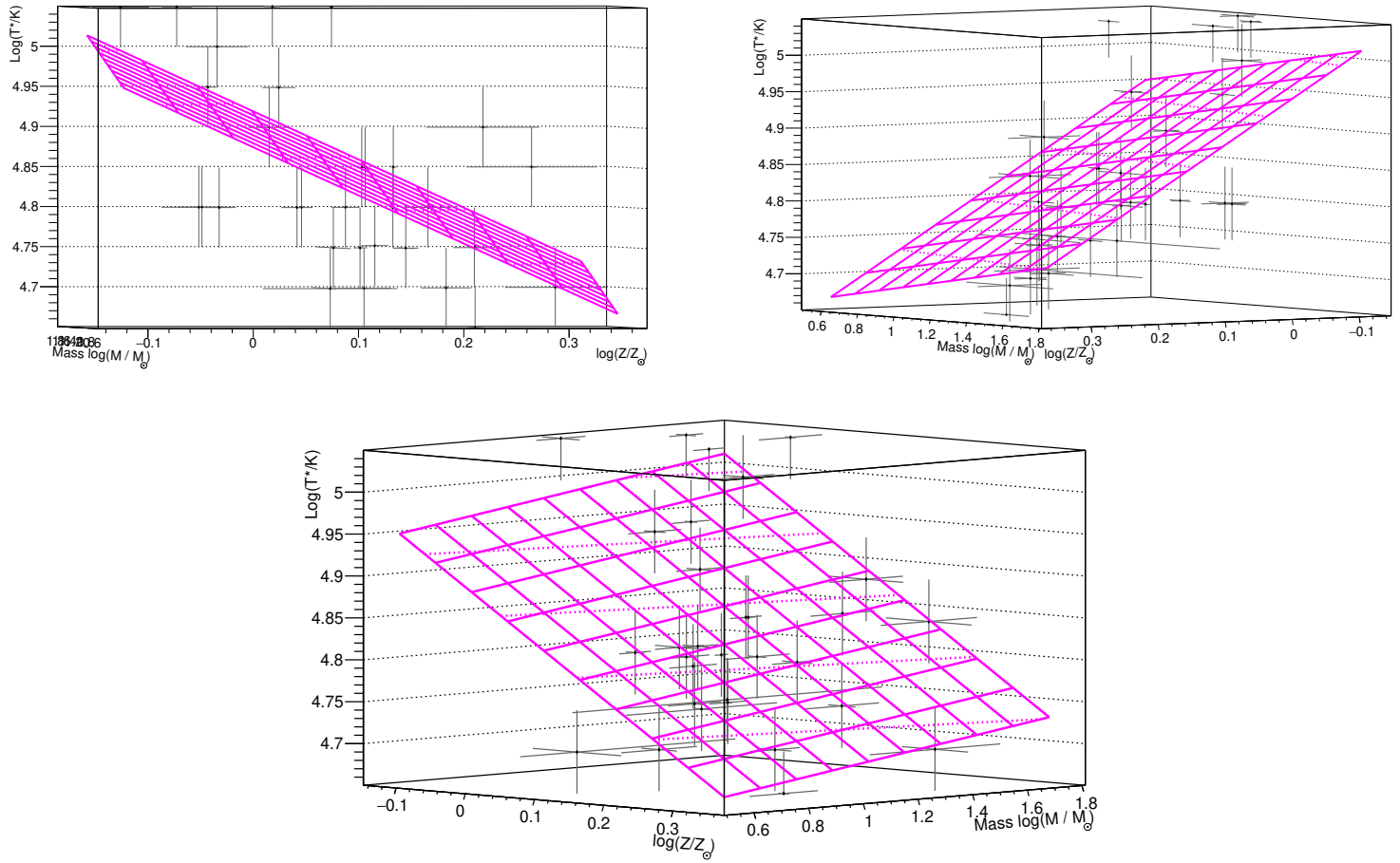


Figure 13: Temperature-mass-metallicity dependence of the WNE stars.

# 4 Summary

Firstly it has to be noted that the improvements of the distance estimates of the stars to the sun have a huge effect on the appearance of the HRD for WNE stars. Hotter stars now are more luminous while cooler stars are found at lower luminosity. Furthermore all WNE stars now lie on the left side of the hydrogen ZAMS line.

The improvements of the luminosity have a direct influence on the mass-loss rate of the stars. Concerning the mass-loss luminosity relation the scatter around the fitted line is considerably reduced. Now that for each star an initial metallicity can be estimated from the present-day radial metallicity gradient, this can also be considered for the mass-loss luminosity relation which is predicted to depend on metallicity too. One derives the formula

$$\log\left(\frac{\dot{M}}{M_{\odot}yr^{-1}}\right) = (-9.16 \pm 0.06) + (0.87 \pm 0.14)\log\left(\frac{L}{L_{\odot}}\right) + (0.80 \pm 0.47)\log\left(\frac{Z}{Z_{\odot}}\right)$$

showing a strong dependence on the luminosity as well as on the metallicity.

At last analyzing the temperature shows it depends more strongly on metallicity than on mass.

$$\log\left(\frac{\mathrm{T}_{*}}{K}\right) = (-0.59 \pm 0.15)\log\left(\frac{Z}{Z_{\odot}}\right) + (0.27 \pm 0.08)\log\left(\frac{M}{M_{\odot}}\right) + (4.57 \pm 0.10)$$

This can be explained by the strong metallicity dependences of the mass-loss rates as well as on the effects that cause a radius inflation of Wolf-Rayet stars. The winds of a Wolf-Rayet stars are line driven winds which strongly depend on heavy elements from the Fe-groups. For higher metallicities one predicts stronger winds which have a direct influence on the mass-loss rate. Almost all Wolf-Rayet stars show an inflated envelope that is much bigger than predicted. In the work of Gräfener et al. (2012), this behavior is explained by iron opacity bump which drives this inflation. The iron opacity bump is directly dependent on the metallicity. These effects influence the structure of Wolf-Rayet stars. In conclusion for WNE stars the temperature depends on the metallicity and as a cause of that the metallicity should be considered as second initial parameter. However the mass needs to be kept as first initial parameter as it defines the structure of a star.

*Acknowledgements*. Special thanks to Götz Gräfener, who gave me good guidance and resources. Also special thanks to Norbert Langer, who helped me not to lose focus and gave me good advices and assistance. This work has made use of data from the European Space Agency (ESA) mission *Gaia* (https://www.cosmos.esa.int/gaia), processed by the *Gaia* Data Processing and Analysis Consortium (DPAC, https://www.cosmos.esa.int/web/gaia/dpac/consortium). Funding for the DPAC has been provided by national institutions, in particular the institutions participating in the *Gaia* Multilateral Agreement.

## References


Anders, F., et al. 2017a, A&A, 597, A30

—. 2017b, A&A, 600, A70

Bailer-Jones, C. A. L., et al. 2018, ArXiv e-prints

Bensby, T., Feltzing, S., & Oey, M. S. 2014, A&A, 562, A71

Bergemann, M. et al. 2014, A&A, 565, A89

Bertelli, G., et al. 1994, Astronomy and Astrophysics, Supplement, 106, 275

Bestenlehner, J. M., et al. 2014, A&A, 570, A38

Cantat-Gaudin, T., et al. 2014, A&A, 569, A17

Carraro, G., et al. 2007, A&A, 476, 217

Crowther, P. A. 2007, Annu. Rev. Astron. Astrophys, 45, 177

Divine, N. 1965, ApJ, 142, 824

Friel, E. D., et al. 2014, A&A, 563, A117

Gaia Collaboration et al. 2018, ArXiv e-prints

Genovali, K., et al. 2014, A&A, 566, A37

Gräfener, G., Owocki, S. P., & Vink, J. S. 2012, A&A, 538, A40

Gräfener, G., et al. 2011, A&A, 535, A56

Hamann, W.-R., Gräfener, G., & Liermann, A. 2006, A&A, 457, 1015

Lamers, H. J. G. L. M., & Cassinelli, J. P. 1999a, Line driven winds (Cambridge University Press), 187–254

—. 1999b, Observations of stellar winds (Cambridge University Press), 8–59

Magrini, L., & Randich, S. 2015, ArXiv e-prints

Magrini, L., et al. 2017, A&A, 603, A2

NASA. 2017, https://www.nasa.gov/mission_pages/sunearth/news/gallery/galaxy-location.html, website, last call: 21.06.2018 9:49pm

Nugis, T., & Lamers, H. J. G. L. M. 2000, A&A, 360, 227

Overbeek, J. C., et al. 2017, A&A, 598, A68

Pols, O. R. 2009a

—. 2009b

Puls, J., Vink, J. S., & Najarro, F. 2008, A&A Rev., 16, 209

Schneider, P. 2004, Einführung in die Extragalaktische Astronomie (Universität Bonn)

Tramper, F., Sana, H., & de Koter, A. 2016, ApJ, 833, 133

van der Hucht, K. A. 2001, New Astronomy Review, 45, 135

# 5 Appendix

| WR | spectral subtype | $d_{\text{est}}$ [kpc] | $d_{\text{est,low}}$ [kpc] | $d_{\text{est,high}}$ [kpc] | $R_{\text{gal}}$ [kpc] | $R_{\text{gal,low}}$ [kpc] | $R_{\text{gal,high}}$ [kpc] |
|---|---|---|---|---|---|---|---|
| 1 | WN4 | 3.17 | 2.87 | 3.54 | 10.05 | 9.83 | 10.32 |
| 2 | WN2 | — | — | — | — | — | — |
| 6 | WN4 | 2.27 | 2.03 | 2.57 | 9.48 | 9.31 | 9.70 |
| 7 | WN4 | 4.32 | 3.66 | 5.22 | 11.36 | 10.81 | 12.14 |
| 18 | WN4 | 4.02 | 3.45 | 4.79 | 8.07 | 7.93 | 8.30 |
| 20 | WN5 | 7.63 | 6.73 | 8.78 | 9.57 | 9.07 | 10.29 |
| 34 | WN5 | 8.82 | 7.55 | 10.53 | 9.67 | 8.92 | 10.82 |
| 36 | WN5 | 6.00 | 5.12 | 7.20 | 8.25 | 7.93 | 8.80 |
| 37 | WN4 | 8.18 | 6.91 | 9.91 | 9.22 | 8.54 | 10.32 |
| 44 | WN4 | 6.55 | 5.63 | 7.78 | 8.31 | 7.95 | 8.92 |
| 46 | WN3 | 2.64 | 2.41 | 2.91 | 7.17 | 7.21 | 7.14 |
| 51 | WN4 | 3.82 | 3.51 | 4.19 | 6.53 | 6.58 | 6.49 |
| 54 | WN5 | 7.18 | 6.04 | 8.76 | 6.79 | 6.48 | 7.48 |
| 55 | WN7 | 3.16 | 2.76 | 3.68 | 6.56 | 6.67 | 6.44 |
| 61 | WN5 | 5.70 | 4.85 | 6.87 | 6.04 | 6.04 | 6.23 |
| 62 | WN6 | 4.97 | 4.18 | 6.07 | 5.73 | 5.88 | 5.72 |
| 63 | WN7 | — | — | — | — | — | — |
| 67 | WN6 | 2.37 | 2.02 | 2.87 | 6.35 | 6.07 | 6.57 |
| 71 | WN6 | 3.21 | 2.82 | 3.73 | 5.80 | 6.02 | 5.53 |
| 74 | WN7 | 5.29 | 4.23 | 6.88 | 4.17 | 4.71 | 3.78 |
| 75 | WN6 | 3.51 | 3.00 | 4.20 | 5.14 | 5.50 | 4.68 |
| 84 | WN7 | 3.27 | 2.84 | 3.85 | 4.87 | 5.27 | 4.34 |
| 91 | WN7 | 5.35 | 4.08 | 7.36 | 2.95 | 4.08 | 1.64 |
| 94 | WN5 | 0.95 | 0.91 | 1.01 | 7.05 | 7.00 | 7.10 |
| 100 | WN5 | 4.05 | 3.30 | 5.20 | 3.97 | 4.71 | 2.83 |
| 107 | WN8 | 5.72 | 3.68 | 8.85 | 2.48 | 1.49 | 4.39 |
| 110 | WN5 | 1.59 | 1.49 | 1.71 | 6.45 | 6.55 | 6.33 |
| 115 | WN6 | 0.57 | 0.33 | 2.01 | 7.46 | 7.68 | 6.11 |
| 120 | WN7 | 1.58 | 1.22 | 2.22 | 6.64 | 6.95 | 6.12 |
| 123 | WN8 | 5.66 | 4.53 | 7.38 | 4.28 | 4.72 | 4.13 |
| 129 | WN4 | 5.91 | 5.02 | 7.14 | 7.79 | 7.54 | 8.30 |
| 134 | WN5 | 1.76 | 1.66 | 1.86 | 7.69 | 7.69 | 7.68 |
| 149 | WN5 | 5.01 | 4.51 | 5.62 | 9.40 | 9.15 | 9.74 |

Table 1: Distance estimates made with ARI (Bailer-Jones et al., 2018) and calculated galactic radii for all hydrogen-free Wolf-Rayet stars

| WR | spectral subtype | $T_*$ [kK] | $\log(L)$ $[L_\odot]$ | $\log(L)_{\text{low}}$ $[L_\odot]$ | $\log(L)_{\text{high}}$ $[L_\odot]$ |
|---|---|---|---|---|---|
| 1 | WN4 | 112.2 | 5.88 | 5.79 | 5.98 |
| 2 | WN2 | 141.3 | — | — | — |
| 6 | WN4 | 89.1 | 5.79 | 5.70 | 5.90 |
| 7 | WN4 | 112.2 | 5.36 | 5.22 | 5.53 |
| 18 | WN4 | 112.2 | 6.11 | 5.98 | 6.26 |
| 20 | WN5 | 63.1 | 5.84 | 5.74 | 5.97 |
| 34 | WN5 | 63.1 | 5.75 | 5.62 | 5.90 |
| 36 | WN5 | 89.1 | 5.30 | 5.16 | 5.45 |
| 37 | WN4 | 100 | 6.05 | 5.90 | 6.21 |
| 44 | WN4 | 79.4 | 5.62 | 5.49 | 5.77 |
| 46 | WN3 | 112.2 | 5.42 | 5.35 | 5.51 |
| 51 | WN4 | 70.8 | 5.50 | 5.43 | 5.58 |
| 54 | WN5 | 63.1 | 5.67 | 5.52 | 5.84 |
| 55 | WN7 | 56.2 | 5.40 | 5.28 | 5.53 |
| 61 | WN5 | 63.1 | 5.03 | 4.89 | 5.19 |
| 62 | WN6 | 70.8 | 5.96 | 5.81 | 6.14 |
| 63 | WN7 | 44.7 | — | — | — |
| 67 | WN6 | 56.6 | 5.11 | 4.97 | 5.28 |
| 71 | WN6 | 56.2 | 5.06 | 4.95 | 5.19 |
| 74 | WN7 | 56.2 | 5.65 | 5.45 | 5.87 |
| 75 | WN6 | 63.1 | 5.59 | 5.45 | 5.75 |
| 84 | WN7 | 50.1 | 5.36 | 5.24 | 5.50 |
| 91 | WN7 | 70.8 | 5.93 | 5.69 | 6.20 |
| 94 | WN5 | 56.2 | 5.52 | 5.48 | 5.57 |
| 100 | WN5 | 79.4 | 5.77 | 5.59 | 5.98 |
| 107 | WN8 | 50.1 | 5.88 | 5.49 | 6.25 |
| 110 | WN5 | 70.8 | 5.51 | 5.45 | 5.57 |
| 115 | WN6 | 50.1 | 4.56 | 4.10 | 5.66 |
| 120 | WN7 | 50.1 | 4.92 | 4.69 | 5.21 |
| 123 | WN8 | 44.7 | 5.28 | 5.08 | 5.51 |
| 129 | WN4 | 63.1 | 5.40 | 5.26 | 5.57 |
| 134 | WN5 | 63.1 | 5.61 | 5.56 | 5.66 |
| 149 | WN5 | 63.1 | 5.43 | 5.34 | 5.53 |

Table 2: Temperature and luminosities for the galactic WNE stars. The luminosity error results from the estimated distances. The temperatures are adopted from Hamann et al. (2006) and their error is one gridspace, which is $\pm \log(0.05)$.

| WR | spectral subtype | $T_*$ [kK] | $\log(L)$ $[L_\odot]$ | $\log(L)_{\text{low}}$ $[L_\odot]$ | $\log(L)_{\text{high}}$ $[L_\odot]$ |
|---|---|---|---|---|---|
| 3 | WN3h | 89.1 | 5.56 | 5.46 | 5.67 |
| 10 | WN5ha | 63.1 | 5.83 | 5.69 | 6.00 |
| 12 | WN8h | 44.7 | 5.98 | 5.84 | 6.14 |
| 16 | WN8h | 44.7 | 5.72 | 5.65 | 5.80 |
| 22 | WN7h | 44.7 | 6.28 | 6.21 | 6.35 |
| 24 | WN6ha | 50.1 | 6.47 | 6.36 | 6.59 |
| 25 | WN6h | 50.1 | 6.38 | 6.32 | 6.44 |
| 28 | WN6(h) | 50.1 | 6.06 | 5.90 | 6.23 |
| 35 | WN6h | 56.2 | 5.69 | 5.57 | 5.83 |
| 40 | WN8h | 44.7 | 5.91 | 5.81 | 6.02 |
| 49 | WN5(h) | 56.2 | 5.40 | 5.26 | 5.56 |
| 66 | WN8(h) | 44.7 | 5.88 | 5.53 | 6.21 |
| 78 | WN7h | 50.1 | 5.80 | 5.73 | 5.88 |
| 82 | WN7(h) | 56.2 | 5.26 | 5.12 | 5.42 |
| 85 | WN6h | 50.1 | 5.38 | 5.28 | 5.48 |
| 87 | WN7h | 44.7 | 6.21 | 6.05 | 6.40 |
| 89 | WN8h | 39.8 | 6.33 | 6.15 | 6.54 |
| 105 | WN9h | 35.5 | 5.89 | 5.78 | 6.01 |
| 108 | WN9h | 39.8 | 5.77 | 5.66 | 5.88 |
| 116 | WN8h | 39.8 | 5.44 | 5.33 | 5.55 |
| 124 | WN8h | 44.7 | 5.75 | 5.57 | 5.95 |
| 128 | WN4(h) | 70.8 | 5.22 | 5.12 | 5.34 |
| 130 | WN8(h) | 44.7 | 6.74 | 6.47 | 7.01 |
| 131 | WN7h | 44.7 | 6.14 | 5.98 | 6.32 |
| 136 | WN6(h) | 70.8 | 5.78 | 5.72 | 5.84 |
| 147 | WN8(h) | 39.8 | 7.38 | 7.09 | 7.66 |
| 148 | WN8h | 39.8 | 6.65 | 6.45 | 6.86 |
| 152 | WN3(h) | 79.4 | 5.24 | 5.09 | 5.43 |
| 156 | WN8h | 39.8 | 6.01 | 5.93 | 6.11 |
| 158 | WN7h | 44.7 | 6.06 | 5.95 | 6.18 |

Table 3: Temperature and luminosities for the galactic WNL stars. The luminosity error results from the estimated distances. The temperatures are adopted from Hamann et al. (2006) and their error is one gridspace, which is $\pm \log(0.05)$.

| WR | spectral subtype | $\log(L)$ $[L_\odot]$ | $\log(L)_{\rm low}$ $[L_\odot]$ | $\log(L)_{\rm high}$ $[L_\odot]$ | $v_\infty$ [km/s] | $\log(\dot{M})$ $[M_\odot yr^{-1}]$ | $\log(\dot{M})_{\rm low}$ $[M_\odot yr^{-1}]$ | $\log(\dot{M})_{\rm high}$ $[M_\odot yr^{-1}]$ |
|---|---|---|---|---|---|---|---|---|
| 1 | WN4 | 5.88 | 5.79 | 5.98 | 1900 | -4.04 | -4.10 | -3.97 |
| 2 | WN2 | — | — | — | 1800 | — | — | — |
| 6 | WN4 | 5.79 | 5.70 | 5.90 | 1700 | -3.85 | -3.93 | -3.77 |
| 7 | WN4 | 5.36 | 5.22 | 5.53 | 1600 | -4.47 | -4.57 | -4.34 |
| 18 | WN4 | 6.11 | 5.98 | 6.26 | 1800 | -3.84 | -3.94 | -3.73 |
| 20 | WN5 | 5.84 | 5.74 | 5.97 | 1200 | -4.22 | -4.30 | -4.12 |
| 34 | WN5 | 5.75 | 5.62 | 5.90 | 1400 | -4.21 | -4.31 | -4.10 |
| 36 | WN5 | 5.30 | 5.16 | 5.45 | 1900 | -4.00 | -4.11 | -3.88 |
| 37 | WN4 | 6.05 | 5.90 | 6.21 | 2150 | -3.89 | -4.00 | -3.76 |
| 44 | WN4 | 5.62 | 5.49 | 5.77 | 1400 | -4.64 | -4.74 | -4.53 |
| 46 | WN3 | 5.42 | 5.35 | 5.51 | 2300 | -5.08 | -5.14 | -5.02 |
| 51 | WN4 | 5.50 | 5.43 | 5.58 | 1500 | -4.70 | -4.75 | -4.64 |
| 54 | WN5 | 5.67 | 5.52 | 5.84 | 1500 | -4.44 | -4.56 | -4.32 |
| 55 | WN7 | 5.40 | 5.28 | 5.53 | 1200 | -4.40 | -4.49 | -4.30 |
| 61 | WN5 | 5.03 | 4.89 | 5.19 | 1400 | -4.68 | -4.78 | -4.55 |
| 62 | WN6 | 5.96 | 5.81 | 6.14 | 1800 | -3.51 | -3.63 | -3.38 |
| 63 | WN7 | — | — | — | 1700 | — | — | — |
| 67 | WN6 | 5.11 | 4.97 | 5.28 | 1500 | -4.52 | -4.62 | -4.39 |
| 71 | WN6 | 5.06 | 4.95 | 5.19 | 1200 | -4.84 | -4.92 | -4.74 |
| 74 | WN7 | 5.65 | 5.45 | 5.87 | 1300 | -4.11 | -4.26 | -3.94 |
| 75 | WN6 | 5.59 | 5.45 | 5.75 | 2300 | -3.88 | -3.98 | -3.76 |
| 84 | WN7 | 5.36 | 5.24 | 5.50 | 1100 | -4.52 | -4.61 | -4.41 |
| 91 | WN7 | 5.93 | 5.69 | 6.20 | 1700 | -3.57 | -3.74 | -3.36 |
| 94 | WN5 | 5.52 | 5.48 | 5.57 | 1300 | -4.46 | -4.49 | -4.43 |
| 100 | WN5 | 5.77 | 5.59 | 5.98 | 1600 | -3.79 | -3.92 | -3.63 |
| 107 | WN8 | 5.88 | 5.49 | 6.25 | 1200 | -3.94 | -4.23 | -3.66 |
| 110 | WN5 | 5.51 | 5.45 | 5.57 | 2300 | -3.88 | -3.92 | -3.83 |
| 115 | WN6 | 4.56 | 4.10 | 5.66 | 1280 | -5.02 | -5.36 | -4.20 |
| 120 | WN7 | 4.92 | 4.69 | 5.21 | 1225 | -4.61 | -4.78 | -4.39 |
| 123 | WN8 | 5.28 | 5.08 | 5.51 | 970 | -4.28 | -4.43 | -4.11 |
| 129 | WN4 | 5.40 | 5.26 | 5.57 | 1320 | -4.72 | -4.83 | -4.60 |
| 134 | WN5 | 5.61 | 5.56 | 5.66 | 1700 | -4.09 | -4.13 | -4.06 |
| 149 | WN5 | 5.43 | 5.34 | 5.53 | 1300 | -4.34 | -4.41 | -4.26 |

Table 4: Corrected luminosities and mass-loss rates and the stellar wind velocity adopted and recalculated from Hamann et al. (2006) with a clumping-factor of $D = 1$.

| WR | spectral subtype | $T_*$ [kK] | $M$ $[M_\odot]$ | $M_{\rm low}$ $[M_\odot]$ | $M_{\rm high}$ $[M_\odot]$ | $Z$ $[Z_\odot]$ | $Z_{\rm low}$ $[Z_\odot]$ | $Z_{\rm high}$ $[Z_\odot]$ |
|---|---|---|---|---|---|---|---|---|
| 1 | WN4 | 112.2 | 26 | 23 | 30 | 0.90 | 0.93 | 0.88 |
| 2 | WN2 | 141.3 | — | — | — | — | — | — |
| 6 | WN4 | 89.1 | 23 | 20 | 27 | 0.96 | 0.98 | 0.94 |
| 7 | WN4 | 112.2 | 13 | 11 | 16 | 0.78 | 0.83 | 0.72 |
| 18 | WN4 | 112.2 | 36 | 30 | 47 | 1.12 | 1.14 | 1.09 |
| 20 | WN5 | 63.1 | 25 | 21 | 29 | 0.95 | 1.00 | 0.88 |
| 34 | WN5 | 63.1 | 22 | 18 | 27 | 0.94 | 1.02 | 0.83 |
| 36 | WN5 | 89.1 | 12 | 10 | 15 | 1.10 | 1.14 | 1.03 |
| 37 | WN4 | 100 | 33 | 27 | 43 | 0.99 | 1.06 | 0.88 |
| 44 | WN4 | 79.4 | 18 | 15 | 22 | 1.09 | 1.14 | 1.02 |
| 46 | WN3 | 112.2 | 14 | 13 | 16 | 1.24 | 1.23 | 1.24 |
| 51 | WN4 | 70.8 | 16 | 14 | 17 | 1.33 | 1.32 | 1.33 |
| 54 | WN5 | 63.1 | 19 | 16 | 25 | 1.29 | 1.33 | 1.19 |
| 55 | WN7 | 56.2 | 14 | 12 | 16 | 1.32 | 1.30 | 1.34 |
| 61 | WN5 | 63.1 | 9 | 8 | 11 | 1.40 | 1.40 | 1.37 |
| 62 | WN6 | 70.8 | 29 | 23 | 38 | 1.45 | 1.42 | 1.45 |
| 63 | WN7 | 44.7 | — | — | — | — | — | — |
| 67 | WN6 | 56.6 | 10 | 8 | 12 | 1.35 | 1.32 | 1.39 |
| 71 | WN6 | 56.2 | 9 | 12 | 17 | 1.44 | 1.40 | 1.48 |
| 74 | WN7 | 56.2 | 19 | 15 | 26 | 1.71 | 1.62 | 1.79 |
| 75 | WN6 | 63.1 | 17 | 15 | 21 | 1.54 | 1.48 | 1.62 |
| 84 | WN7 | 50.1 | 13 | 11 | 16 | 1.59 | 1.52 | 1.68 |
| 91 | WN7 | 70.8 | 28 | 20 | 42 | 1.96 | 1.73 | 2.26 |
| 94 | WN5 | 56.2 | 16 | 33 | 59 | 1.25 | 1.25 | 1.26 |
| 100 | WN5 | 79.4 | 22 | 17 | 30 | 1.75 | 1.62 | 1.98 |
| 107 | WN8 | 50.1 | 26 | 15 | 17 | 2.06 | 1.67 | 2.30 |
| 110 | WN5 | 70.8 | 16 | 15 | 17 | 1.34 | 1.32 | 1.35 |
| 115 | WN6 | 50.1 | 5 | 3 | 19 | 1.20 | 1.17 | 1.39 |
| 120 | WN7 | 50.1 | 8 | 6 | 11 | 1.31 | 1.27 | 1.39 |
| 123 | WN8 | 44.7 | 12 | 9 | 16 | 1.69 | 1.61 | 1.72 |
| 129 | WN4 | 63.1 | 14 | 12 | 17 | 1.15 | 1.19 | 1.09 |
| 134 | WN5 | 63.1 | 18 | 17 | 19 | 1.17 | 1.17 | 1.17 |
| 149 | WN5 | 63.1 | 14 | 13 | 16 | 0.97 | 1.00 | 0.93 |

Table 5: Temperature, mass and metallicity for all galactic WNE stars.